Featured in Physics

Crystal Nucleation in Supercooled Atomic Liquids

Johannes Möller,[1,*] Alexander Schottelius,[2,*] Michele Caresana,[2] Ulrike Boesenberg,[1] Chan Kim,[1] Francesco Dallari,[3,‡] Tiberio A. Ezquerra,[4] José M. Fernández,[5] Luca Gelisio,[3,§] Andrea Glaesener,[6] Claudia Goy,[3] Jörg Hallmann,[1] Anton Kalinin,[7] Ruslan P. Kurta,[1] Dmitry Lapkin,[3,‖] Felix Lehmkühler,[3] Francesco Mambretti,[6,¶] Markus Scholz,[1] Roman Shayduk,[1] Florian Trinter,[2,3,8] Ivan A. Vartaniants,[3] Alexey Zozulya,[1] Davide E. Galli,[6] Gerhard Grübel,[3,9,**] Anders Madsen,[1] Frédéric Caupin,[10] and Robert E. Grisenti[2,7,†]

[1]*European X-ray Free-Electron Laser Facility, 22869 Schenefeld, Germany*
[2]*Institut für Kernphysik, Goethe-Universität Frankfurt am Main, 60438 Frankfurt am Main, Germany*
[3]*Deutsches Elektronen-Synchrotron DESY, 22607 Hamburg, Germany*
[4]*Macromolecular Physics Department, Instituto de Estructura de la Materia, IEM-CSIC, 28006 Madrid, Spain*
[5]*Laboratory of Molecular Fluid Dynamics, Instituto de Estructura de la Materia, IEM-CSIC, 28006 Madrid, Spain*
[6]*Dipartimento di Fisica "Aldo Pontremoli," Università degli Studi di Milano, 20133 Milano, Italy*
[7]*GSI Helmholtzzentrum für Schwerionenforschung GmbH, 64291 Darmstadt, Germany*
[8]*Molecular Physics, Fritz-Haber-Institut der Max-Planck-Gesellschaft, 14195 Berlin, Germany*
[9]*The Hamburg Centre for Ultrafast Imaging, 22761 Hamburg, Germany*
[10]*Institut Lumière Matière, Université Claude Bernard Lyon 1, CNRS, Institut Universitaire de France, 69622 Villeurbanne, France*

(Received 29 September 2023; revised 22 February 2024; accepted 28 March 2024; published 17 May 2024)

The liquid-to-solid phase transition is a complex process that is difficult to investigate experimentally with sufficient spatial and temporal resolution. A key aspect of the transition is the formation of a critical seed of the crystalline phase in a supercooled liquid, that is, a liquid in a metastable state below the melting temperature. This stochastic process is commonly described within the framework of classical nucleation theory, but accurate tests of the theory in atomic and molecular liquids are challenging. Here, we employ femtosecond x-ray diffraction from microscopic liquid jets to study crystal nucleation in supercooled liquids of the rare gases argon and krypton. Our results provide stringent limits to the validity of classical nucleation theory in atomic liquids, and offer the long-sought possibility of testing nonclassical extensions of the theory.

DOI: 10.1103/PhysRevLett.132.206102

Crystallization, one of the most fundamental phase transitions, is classically viewed as a two-step process. Through a mechanism commonly known as homogeneous crystal nucleation, thermal fluctuations in a supercooled liquid trigger the spontaneous formation of a critical, localized seed of the emerging ordered phase, which subsequently grows to macroscopic dimensions. Crystal nucleation plays a crucial role, for example, in the description of ice formation in tropospheric clouds of Earth's atmosphere [1,2] and accretion of Earth's inner core [3]. Microscopically, homogeneous crystal nucleation is described in the framework of classical nucleation theory (CNT) [4,5]. Although nonclassical approaches to crystal nucleation have received increased attention in recent years [5–15], there is still a debate about the limits of validity of CNT, both in supercooled liquids as well as in unconventional condensed-matter systems [16]. Identifying the systems for which CNT is valid would be important to develop more sophisticated models of crystal nucleation starting from the classical theory [11,17].

One of the most important observables that can be calculated in CNT is the temperature (T) dependent crystal nucleation rate $J(T)$, which represents the probability of formation of a crystal seed per unit time and volume. It is given by $J(T) = n(T)\kappa(T)\exp\left[-\Delta G^*(T)/k_B T\right]$ [4], where $n(T)$ is the volume number density of particles in the liquid, $\kappa(T)$ is a kinetic factor, $\Delta G^*(T)$ is the free-energy barrier for critical crystal seed formation, and k_B is Boltzmann's constant. The crystal nucleation rate sets the lifetime $\tau(T)$ of a liquid sample of volume V according to $\tau(T) = [J(T)V]^{-1}$. A measurement of $J(T)$ in atomic and molecular systems is challenging because at low temperatures $\tau(T)$ can be very short, from nanoseconds to picoseconds, thereby requiring extremely fast probing of microscopic metastable liquid samples. In addition, studies of homogeneous crystal nucleation require the use of liquid samples free of any contaminating particles to avoid heterogeneous nucleation. The latter condition, however, is difficult to establish reliably in experiments, thus potentially leading to conflicting results [18,19]. When experimental homogeneous crystal nucleation rates are available, quantitative comparison with CNT remains uncertain because $J(T)$ depends on many thermodynamic parameters, such as the crystal-liquid interfacial free energy γ, which are often

difficult to determine with sufficient accuracy. For example, an uncertainty by less than 5% in γ can lead to variations in the determination of $J(T)$ by many orders of magnitude [20–23].

An alternative route to estimating $J(T)$ is provided by molecular dynamics simulations [24], which offer a connection between experiments and modeling. With few exceptions [25,26], however, persistent inconsistencies between experimental and simulated crystal nucleation rates still prevent this approach from being fully exploited for the study of homogeneous crystal nucleation [27]. A prominent example that illustrates this impasse is supercooled water, where simulated nucleation rates can differ from those measured experimentally by 10 orders of magnitude [28]. It is believed that the inherent limitations of the empirical models used to describe particle interactions contribute substantially to the observed discrepancies [27].

Lennard-Jones (LJ) liquids are the simplest atomic model systems and thus of particular interest for molecular dynamics simulations. They allow avoiding the problems arising from complex interactions, and the simple, isotropic LJ potential makes simulations exceedingly fast. Therefore, despite the challenges associated with the stochastic nature of crystal nucleation in terms of very long computational time scales, the simulation of the entire crystallization process, from formation of the critical seed in the supercooled liquid to crystal growth, was successfully performed for a LJ liquid [29]. Recently, crystal nucleation rates from molecular dynamics simulations of supercooled LJ liquids have been reported for a wide range of temperatures [30–32], suggesting the validity of CNT in these systems.

Here, we investigated experimentally crystal nucleation in supercooled liquids of the atomic elements argon and krypton. The interatomic interactions in condensed heavy rare gases are well described by LJ potentials [33]. Hence, our results set new benchmarks for simulated crystal nucleation rates and thus for assessment of CNT. To investigate the early stages of crystallization from the supercooled state we used microscopic liquid jets of argon and krypton in a vacuum. A vacuum-exposed jet rapidly cools by surface evaporation well below the melting temperature before it eventually starts crystallizing with the onset of homogeneous crystal nucleation [34–36]. The crystal formation can then be effectively probed by femtosecond x-ray pulses [37], obtaining single-pulse diffraction patterns that contain microscopic structural details of the growing crystals.

The experiments were performed at the Materials Imaging and Dynamics (MID) instrument at the European X-ray Free-Electron Laser Facility [38]. The liquid jets were generated by condensation of 99.999% purity argon or krypton gas in a cryogenically cooled glass-capillary nozzle with diameter $d_0 = 3.5 \pm 0.5$ μm. The source pressures and temperatures were $P_0 = 70 \pm 1$ bar and $T_0 = 93 \pm 0.5$ K, respectively,

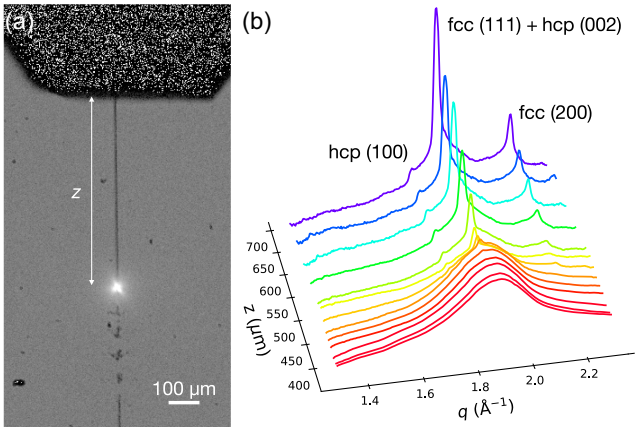

FIG. 1. (a) Stroboscopic image of the 3.5 μm-diameter krypton jet. The interaction with the focused x-ray beam resulted in plasma formation, visible as bright spot on the continuous filament, followed by vaporization of a segment of the jet. The trigger of the nanosecond laser-based background illumination was set to record an image of the jet after every fifth x-ray pulse. (b) Selection of azimuthally integrated and background-subtracted, powderlike diffraction profiles measured with the krypton jet. The labeled peaks represent reflections of the fcc and hcp crystal structures.

for argon and $P_0 = 70 \pm 1$ bar and $T_0 = 123.7 \pm 0.5$ K for krypton. Under these experimental conditions the flow was laminar and the jet velocity, an important parameter in this Letter, is therefore given by the Bernoulli equation $v = \sqrt{2P_0/\rho(T_0)}$ [39], where $\rho(T_0)$ is the density of the liquid, obtaining $v = 101 \pm 1$ m s^{-1} for the argon jet and $v = 76 \pm 1$ m s^{-1} for the krypton jet. The custom-built liquid-jet source was mounted on a hexapod in the multipurpose vacuum chamber of MID, allowing a three-dimensional displacement and tilting of the liquid jet. The jets were probed by 9.7 keV x-ray pulses with < 25 fs duration focused down to a spot on the sample with diameter (FWHM) $d = 300 \pm 100$ nm. The x-ray pulses were delivered in 10 Hz pulse trains, with each train consisting of 50 individual pulses at a repetition rate of 1.14 MHz. A stroboscopic image of the krypton jet hit by the x rays is shown in Fig. 1(a). The self-replenishing nature of the liquid jet allowed us to take advantage of the MHz repetition mode of the European X-ray Free-Electron Laser Facility, delivering a fresh sample at a comparable rate. The scattered x rays were recorded by the adaptive gain integrating pixel detector (AGIPD) [40], covering the ≈1.4–2.3 Å^{-1} range of the modulus of the photon wave vector transfer $q = (4\pi/\lambda)\sin(\Theta/2)$, where λ is the radiation wavelength and Θ the scattering angle. Spatial scans were recorded as a function of the distance z from the nozzle exit, and for each z we recorded $> 10^6$ single-pulse diffraction images. The determination of z was based on the analysis of integrated pixel intensities of CCD camera images of the liquid jet as shown in Fig. 1(a). Here, the positions of both the nozzle orifice and the x-ray beam spot are visible, so their relative

distance could be determined accurately (see Supplemental Material [41]). Analysis of the CCD images also allowed us to validate the accuracy of the Bernoulli equation in predicting the jet velocity [41].

Figure 1(b) shows a selection of background-subtracted, powderlike diffraction profiles $\langle I(q)\rangle$, obtained by azimuthal integration of averaged single-pulse diffraction images from the krypton jet [41]. Close to the nozzle, $\langle I(q)\rangle$ exhibits a broad peak characteristic of the disordered liquid phase. As z increases, the reduction of this broad component, accompanied by the appearance and subsequent rise of sharp diffraction peaks, are distinct features of jet crystallization [36]. The three visible peaks are the (111) and (200) reflections of the face-centered cubic (fcc) crystal and the (100) and (002) reflections of the hexagonal close-packed (hcp) crystal, with the (111) and (002) peaks appearing at the same q. The presence of both fcc and hcp reflections likely results from the formation of crystals with random stacking order or the coexistence of fcc and hcp crystalline domains [29], and reflects the small energy difference between the two crystal structures.

To reliably identify the weak intensity scattered by small crystals, we developed a data-reduction scheme to remove instrument background, liquid scattering contributions, and baseline drifts of the AGIPD. This allowed the identification of crystal diffraction even in the presence of a dominating liquid scattering signal. Details on the reduction procedure are described in the Supplemental Material [41]. A diffraction pattern obtained from summation of 3.4×10^4 reduced single-pulse images measured with the krypton jet at $z = 695.8$ μm is shown in Fig. 2(a). It exhibits characteristic powderlike Debye-Scherrer rings of the fcc and hcp crystals. Yet the single-pulse images reveal more complex diffraction patterns, as shown in Fig. 2(b), displaying not only intense Bragg spots, but also intensity streaks. The latter features directly result from a modification of the three-dimensional intensity distribution in reciprocal space [48,49], and have their microscopic origin in structural defects such as stacking faults and twin boundaries [50].

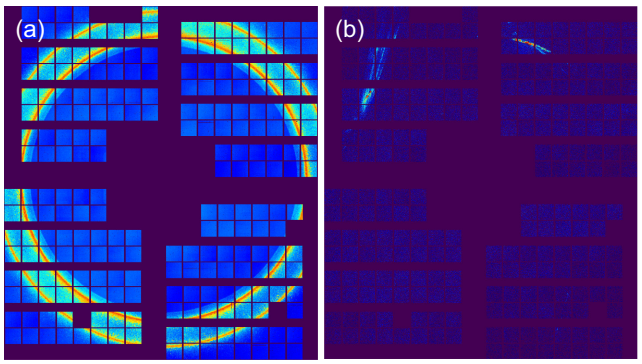

FIG. 2. (a) Powderlike diffraction pattern obtained from 3.4×10^4 reduced single-pulse exposures of the AGIPD measured with the krypton jet at $z = 695.8$ μm. The three visible Debye-Scherrer rings are reflections of the fcc and hcp crystals, as shown in Fig. 1(b), with the weak, innermost ring representing the hcp (100) reflection. (b) Example of a reduced single-pulse image, showing both Bragg peaks and intensity streaks.

The primary experimental observable in this Letter, directly related to crystal nucleation, is the fraction ϕ of single-pulse images at each distance containing distinct crystal features as in Fig. 2(b), plotted for the argon and krypton jets in Figs. 3(a) and 3(b), respectively. The measured ϕ values may be biased by the sensitivity of the AGIPD to single-shot crystal detection, particularly at the smallest distances where ϕ is small. We note, however, that in experiments on x-ray scattering from water droplets only a negligible fraction of undetected ice was estimated [37]. The results shown in Fig. 3 were obtained by considering only the first x-ray pulse of each train, thereby reducing the number of diffraction patterns actually used in the analysis to about 10^4. For the remaining 49 pulses in the train we found slightly different values of ϕ. This observation can be rationalized by the propagation along the jet direction of shock waves generated by the x-ray pulses [51]. The time interval between two pulse trains (≈100 ms) was sufficient for complete jet recovery, but not that between two successive pulses (≈0.9 μs) within a train, as shown in Fig. 1(a). The pressure in the shock wave can be high [52], up to $\sim 10^4$ greater than the Laplace pressure of $\sigma/d_0 \sim 10^{-2}$ bar, where σ is the surface tension, in the unperturbed liquid jet, thereby suggesting a different crystal nucleation pathway at high pressures.

In general, the probability $\Sigma(t)$ that no nucleation event has occurred in a sample of constant volume after a time t is given by [20,53]

$$\ln \Sigma(t) = -V \int_0^t J(t')\mathrm{d}t', \tag{1}$$

where the integral indicates that a nonstationary crystal nucleation rate is considered. Because we were effectively probing at time $t = z/v$, it is possible to identify $1 - \Sigma(z)$ with ϕ and, hence, use Eq. (1) to infer $J(T)$ [54]. To convert distance to temperature, one might approximate T by the average temperature of the crystals that generated the Bragg peaks in the diffraction patterns [41], shown as symbols for the argon and krypton jets in Figs. 3(c) and 3(d), respectively. However, these temperatures may differ from those of the liquid at the onset of jet crystallization because of the latent heat released during crystal formation, and so a combined analysis of crystal nucleation and heat transfer is required to deduce the actual temperatures [55].

Here, we used Knudsen's kinetic theory of evaporation to compute accurately the temperature of the liquid jet [34,37,53,55,56]. The jet is approximated by a cylinder divided into N concentric shells of uniform volume,

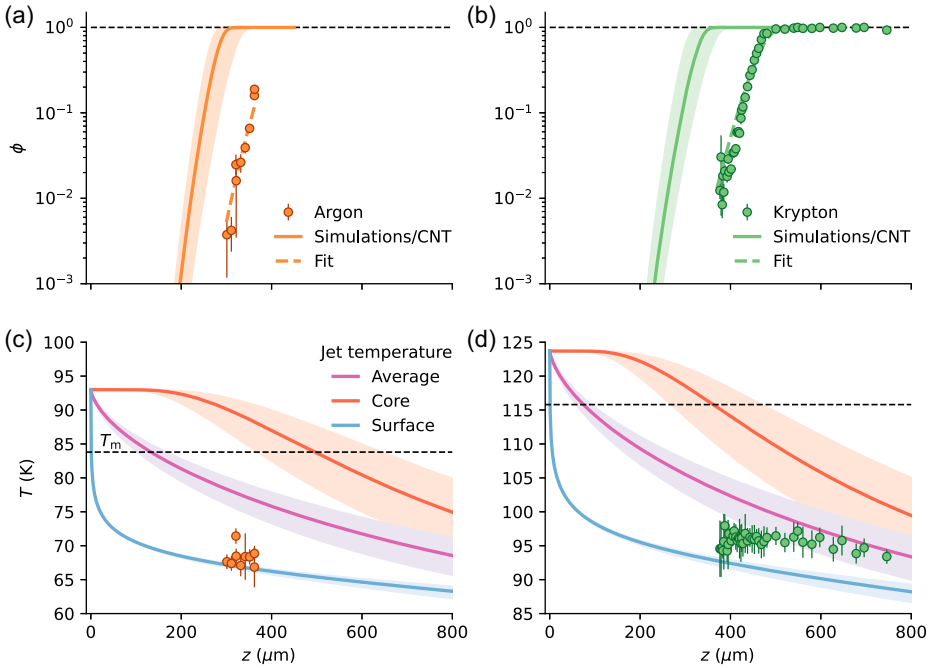

FIG. 3. (a),(b) The symbols represent the measured ϕ values for the argon (a) and krypton (b) jets. The error bars account for different assumptions in the data-reduction scheme [41]. The solid lines are plots of Eq. (2) with $J(T)$ given by Eq. (3), with the shaded regions representing the overall effect of the experimental uncertainties in nozzle diameter and jet velocity, and the variation of the crystal growth rate between 10 and 25 $\mathrm{m\,s^{-1}}$ for argon and between 15 and 20 $\mathrm{m\,s^{-1}}$ for krypton. The dashed lines are fits of Eq. (2) to the experimental data with c in Eq. (3) as fitting parameter. The black dashed lines represent $\phi = 1$. (c),(d) The purple, red, and blue solid lines represent the average temperature and the temperatures of the inner and outermost shells, respectively, computed on the basis of Knudsen's model of evaporative cooling for the argon (c) and krypton (d) jets. The shaded regions represent variations resulting from the uncertainties in nozzle diameter and jet velocity. The symbols represent the estimated temperatures of the crystals at the onset of crystallization of the argon (c) and krypton (d) jets as described in the Supplemental Material [41]. The melting temperatures of argon and krypton are shown as dashed lines.

allowing for evaporative cooling of the outermost shell. The model then yields, as a function of z, the temperatures $T_i(z)$, $i = 1, \ldots, N$, of the individual shells. Knudsen's model has been described in detail elsewhere [37,53,55], with all relevant thermodynamic parameters of argon and krypton provided in the Supplemental Material [41]. The computed average temperature and the temperatures of the inner and outermost shells are shown in Fig. 3(c) for the argon jet and in Fig. 3(d) for the krypton jet as purple, red, and blue solid lines, respectively. In these computations we used $N = 70$ [41]. The marked temperature gradient between the surface and the center of the jet results from the finite thermal conduction that governs heat exchange inside the jet [34,53,55]. We note that the estimated temperatures of the crystals [41] in Figs. 3(c) and 3(d) suggest that they primarily formed in the outer, colder regions of the jet.

In view of the radial dependence of the jet temperature, we deduced from Eq. (1) a theoretical fraction $\phi(z)$ that takes into account the crystal nucleation rate in each cylindrical shell at its current computed temperature $T_i(z)$ [41,53],

$$\phi(z) = 1 - \exp\left\{-\frac{1}{v}\int_0^z \sum_{i=1}^{N} J[T_i(z')]V_i(z,z')\mathrm{d}z'\right\}, \quad (2)$$

being $V_i(z,z')$ the common volume of the ith shell and a cylinder with diameter $d + 2(u/v)(z - z')$, and where the second term in the last expression takes into account the finite crystal growth rate u. The full calculation of $V_i(z,z')$ is presented in the Supplemental Material [41]. Provided that a parameter-free model for the crystal nucleation rate is available, Eq. (2) thus allows for direct comparison between theory and experiments.

As choice for $J(T)$, we assumed recent crystal nucleation rates calculated using the CNT equations with the thermodynamic parameters inferred from molecular dynamics simulations of a LJ liquid [31] with the parameters of argon and krypton [57],

$$\ln[J(T)/(\mathrm{m^{-3}\,s^{-1}})] = c - 1.2829\left(\frac{T}{T_\mathrm{m}}\right)^{-1}\left(1-\frac{T}{T_\mathrm{m}}\right)^{-2}, \quad (3)$$

where $c = 98.2$ for argon and $c = 97.7$ for krypton, and $T_\mathrm{m} = 83.8$ K and $T_\mathrm{m} = 115.8$ K being the melting

temperatures of argon and krypton, respectively. The temperature dependence of Eq. (3) is that derived in CNT using an approximation of $J(T)$ [31], with $c = \ln[n(T)\kappa(T)]$ independent of T. The plots of Eq. (2) with $J(T)$ given by Eq. (3) are shown for the argon and krypton jets as solid lines in Figs. 3(a) and 3(b), respectively. In evaluating $V_i(z, z')$, we neglected for simplicity the variation of the crystal growth rate with temperature [36], assuming $u = 25\ \mathrm{m\,s^{-1}}$ for argon and $u = 20\ \mathrm{m\,s^{-1}}$ for krypton. We verified that a different choice of u in a realistic range of values for the two liquids [36] only had a minor effect, which we included in the estimation of the total uncertainties shown as shaded regions in Figs. 3(a) and 3(b).

To express the differences between the experimental results and the theoretical predictions in Figs. 3(a) and 3(b) more quantitatively, we fitted Eq. (2) to the measured ϕ values using c in Eq. (3) as fitting parameter, with the fits shown as dashed lines. We found $c = 92.1^{+2.2}_{-1.5}$ for argon and $c = 91.3^{+1.8}_{-2.2}$ for krypton, which show that the crystal nucleation rates predicted on the basis of molecular dynamics simulations and CNT are by a factor of 50–1000 for argon and 100–5000 for krypton larger than those inferred from our experimental data. These are the most stringent limits available to date on the accuracy of CNT in supercooled atomic liquids.

Several models of homogeneous crystal nucleation beyond CNT have been proposed, for example assuming more realistic hypotheses with respect to the ideal spherical shape of the critical nucleus in CNT [6,8]. It has also been argued that the classical theory represents the limit of a more general non-Markovian framework [9]. Two-step nucleation scenarios, involving the initial formation of precritical clusters structurally in a thermodynamically metastable state, offer a further, widely debated extension of CNT [11–15]. Overall, our results indicate that any effects related to such corrections must be on the order of the differences between experiments and theory in Figs. 3(a) and 3(b). We therefore expect that our approach will allow exploring the implications of different extensions of CNT on the estimation of crystal nucleation rates in the simple supercooled liquids of the present Letter. Ultimately, the probing of liquid jets of argon and krypton using femtosecond x-ray pulses, as demonstrated here, promises to advance our current understanding of crystallization.

Data recorded during the experiment is available at [58].

We acknowledge financial support by the Bundesministerium für Bildung und Forschung (BMBF), Project No. 05K16RF2, and the Deutsche Forschungsgemeinschaft (DFG), Project No. 499455518. We acknowledge the European XFEL in Schenefeld, Germany, for provision of x-ray free-electron laser beam time at the MID instrument of the SASE-2 beamline and thank all staff for assistance. We also acknowledge support by the Centre for Molecular Water Science (CMWS) at DESY in Hamburg, Germany. F. L. and G. G. acknowledge support by the DFG Cluster of Excellence EXC 2056, "Advanced Imaging of Matter," Project No. 390715994. F. T. acknowledges support by the MaxWater initiative of the Max-Planck-Gesellschaft. We thank Azat Tipeev at the Universidade Federal in São Carlos, Brazil, for providing us the analytical expression representing the theoretical crystal nucleation rates, Eq. (3), and for a careful reading of the manuscript. We thank Jolanta Sztuk-Dambietz and Natascha Raab for their support in running the AGIPD and for discussions on data correction.

*These authors contributed equally to this work.
†Corressponding author: grisenti@atom.uni-frankfurt.de
‡Present address: Dipartimento di Fisica e Astronomia "Galileo Galilei," Università degli Studi di Padova, 35131 Padova, Italy.
§Present address: European X-ray Free-Electron Laser Facility, 22869 Schenefeld, Germany.
‖Present address: Institut für Angewandte Physik, Universität Tübingen, 72076 Tübingen, Germany.
¶Present address: Istituto Italiano di Tecnologia, 16152 Genova, Italy.
**Present address: European X-ray Free-Electron Laser Facility, 22869 Schenefeld, Germany.

[1] W. Cantrell and A. Heymsfield, Production of ice in tropospheric clouds: A review, Bull. Am. Meteorol. Soc. **86**, 795 (2005).
[2] R. J. Herbert, B. J. Murray, S. J. Dobbie, and T. Koop, Sensitivity of liquid clouds to homogenous freezing parameterizations, Geophys. Res. Lett. **42**, 1599 (2015).
[3] L. Huguet, J. A. Van Orman, S. A. Hauck II, and M. A. Willard, Earth's inner core nucleation paradox, Earth Planet. Sci. Lett. **487**, 9 (2018).
[4] K. F. Kelton and A. L. Greer, *Nucleation in Condensed Matter* (Elsevier, New York, 2010).
[5] S. Karthika, T. K. Radhakrishnan, and P. Kalaichelvi, A review of classical and nonclassical nucleation theories, Cryst. Growth Des. **16**, 6663 (2016).
[6] S. Prestipino, A. Laio, and E. Tosatti, Systematic improvement of classical nucleation theory, Phys. Rev. Lett. **108**, 225701 (2012).
[7] P. J. M. Smeets, A. R. Finney, W. J. E. M. Habraken, F. Nudelman, H. Friedrich, J. Laven, J. J. De Yoreo, P. M. Rodger, and N. A. J. M. Sommerdijk, A classical view on nonclassical nucleation, Proc. Natl. Acad. Sci. U.S.A. **114**, E7882 (2017).
[8] J. F. Lutsko, Systematically extending classical nucleation theory, New J. Phys. **20**, 103015 (2018).
[9] A. Kuhnhold, H. Meyer, G. Amati, P. Pelagejcev, and T. Schilling, Derivation of an exact, nonequilibrium framework for nucleation: Nucleation is *a priori* neither diffusive nor Markovian, Phys. Rev. E **100**, 052140 (2019).
[10] A. S. Abyzov, J. W. P. Schmelzer, V. M. Fokin, and E. D. Zanotto, Crystallization of supercooled liquids:

Self-consistency correction of the steady-state nucleation rate, Entropy **22**, 558 (2020).
[11] D. Kashchiev, Classical nucleation theory approach to two-step nucleation of crystals, J. Cryst. Growth **530**, 125300 (2020).
[12] F. Leoni and J. Russo, Nonclassical nucleation pathways in stacking-disordered crystals, Phys. Rev. X **11**, 031006 (2021).
[13] R. K. Bowles and P. Harrowell, Influence on crystal nucleation of an order-disorder transition among the subcritical clusters, Phys. Rev. E **105**, L062602 (2022).
[14] Y.-C. Hu and H. Tanaka, Revealing the role of liquid preordering in crystallisation of supercooled liquids, Nat. Commun. **13**, 4519 (2022).
[15] J. Rogal and G. Díaz Leines, Controlling crystallization: What liquid structure and dynamics reveal about crystal nucleation mechanisms, Phil. Trans. R. Soc. A **381**, 20220249 (2023).
[16] L. Jin, Y. Shi, F. I. Allen, L.-Q. Chen, and J. Wu, Probing the critical nucleus size in the metal-insulator phase transition of VO_2, Phys. Rev. Lett. **129**, 245701 (2022).
[17] D. Eaton, I. Saika-Voivod, R. K. Bowles, and P. H. Poole, Free energy surface of two-step nucleation, J. Chem. Phys. **154**, 234507 (2021).
[18] J. Bokeloh, R. E. Rozas, J. Horbach, and G. Wilde, Nucleation barriers for the liquid-to-crystal transition in Ni: Experiment and simulation, Phys. Rev. Lett. **107**, 145701 (2011).
[19] A. Filipponi, A. De Cicco, S. De Panfilis, P. Giammatteo, and F. Iesari, Crystalline nucleation in undercooled liquid nickel, Acta Mater. **124**, 261 (2017).
[20] B. Riechers, F. Wittbracht, A. Hütten, and T. Koop, The homogeneous ice nucleation rate of water droplets produced in a microfluidic device and the role of temperature uncertainty, Phys. Chem. Chem. Phys. **15**, 5873 (2013).
[21] L. Ickes, A. Welti, C. Hoose, and U. Lohmann, Classical nucleation theory of homogeneous freezing of water: Thermodynamic and kinetic parameters, Phys. Chem. Chem. Phys. **17**, 5514 (2015).
[22] T. Koop and B. J. Murray, A physically constrained classical description of the homogeneous nucleation of ice in water, J. Chem. Phys. **145**, 211915 (2016).
[23] A. O. Tipeev, E. D. Zanotto, and J. P. Rino, Crystal nucleation kinetics in supercooled germanium: MD simulations versus experimental data, J. Phys. Chem. B **124**, 7979 (2020).
[24] G. C. Sosso, J. Chen, S. J. Cox, M. Fitzner, P. Pedevilla, A. Zen, and A. Michaelides, Crystal nucleation in liquids: Open questions and future challenges in molecular dynamics simulations, Chem. Rev. **116**, 7078 (2016).
[25] Y. Sun, H. Song, F. Zhang, L. Yang, Z. Ye, M. I. Mendelev, C.-Z. Wang, and K.-M. Ho, Overcoming the time limitation in molecular dynamics simulation of crystal nucleation: A persistent-embryo approach, Phys. Rev. Lett. **120**, 085703 (2018).
[26] L. G. V. Gonçalves, J. P. B. de Souza, and E. D. Zanotto, Assessment of the classical nucleation theory in supercooled nickel by molecular dynamics, Mater. Chem. Phys. **272**, 125011 (2021).
[27] K. E. Blow, D. Quigley, and G. C. Sosso, The seven deadly sins: When computing crystal nucleation rates, the devil is in the details, J. Chem. Phys. **155**, 040901 (2021).
[28] A. Haji-Akbari and P. G. Debenedetti, Direct calculation of ice homogeneous nucleation rate for a molecular model of water, Proc. Natl. Acad. Sci. U.S.A. **112**, 10582 (2015).
[29] W. Ouyang, B. Sun, Z. Sun, and S. Xu, Entire crystallization process of Lennard-Jones liquids: A large-scale molecular dynamics study, J. Chem. Phys. **152**, 054903 (2020).
[30] V. G. Baidakov and A. O. Tipeev, Crystal nucleation and the solid-liquid interfacial free energy, J. Chem. Phys. **136**, 074510 (2012).
[31] A. O. Tipeev, E. D. Zanotto, and J. P. Rino, Diffusivity, interfacial free energy, and crystal nucleation in a supercooled Lennard-Jones liquid, J. Phys. Chem. C **122**, 28884 (2018).
[32] V. G. Baidakov and K. R. Protsenko, Spontaneous crystallization of a supercooled Lennard-Jones liquid: Molecular dynamics simulation, J. Phys. Chem. B **123**, 8103 (2019).
[33] P. Schwerdtfeger, A. Burrows, and O. R. Smits, The Lennard-Jones potential revisited: Analytical expressions for vibrational effects in cubic and hexagonal close-packed lattices, J. Phys. Chem. A **125**, 3037 (2021).
[34] M. Kühnel, J. M. Fernández, G. Tejeda, A. Kalinin, S. Montero, and R. E. Grisenti, Time-resolved study of crystallization in deeply cooled liquid parahydrogen, Phys. Rev. Lett. **106**, 245301 (2011).
[35] R. E. Grisenti, A. Kalinin, C. Goy, and A. Schottelius, Evaporating laminar microjets for studies of rapidly evolving structural transformations in supercooled liquids, Adv. Phys. X **3**, 1418183 (2018).
[36] A. Schottelius, F. Mambretti, A. Kalinin, B. Beyersdorff, A. Rothkirch, C. Goy, J. Müller, N. Petridis, M. Ritzer, F. Trinter, J. M. Fernández, T. A. Ezquerra, D. E. Galli, and R. E. Grisenti, Crystal growth rates in supercooled atomic liquid mixtures, Nat. Mater. **19**, 512 (2020).
[37] J. A. Sellberg *et al.*, Ultrafast x-ray probing of water structure below the homogeneous ice nucleation temperature, Nature (London) **510**, 381 (2014).
[38] A. Madsen, J. Hallmann, G. Ansaldi, T. Roth, W. Lu, C. Kim, U. Boesenberg, A. Zozulya, J. Möller, R. Shayduk, M. Scholz, A. Bartmann, A. Schmidt, I. Lobato, K. Sukharnikov, M. Reiser, K. Kazarian, and I. Petrov, Materials imaging and dynamics (MID) instrument at the European x-ray free-electron laser facility, J. Synchrotron Radiat. **28**, 637 (2021).
[39] R. A. Costa Fraga, Entwicklung und Charakterisierung mikroskopischer, kryogener Tröpfchentargets für die Anwendung in Experimenten der Laserplasma- und Atomphysik, Ph.D. thesis, Johann Wolfgang Goethe-Universität, Frankfurt am Main, Germany, 2015.
[40] A. Allahgholi *et al.*, Megapixels@Megahertz—The AGIPD high-speed cameras for the European XFEL, Nucl. Instrum. Methods Phys. Res., Sect. A **942**, 162324 (2019).
[41] See Supplemental Material at http://link.aps.org/supplemental/10.1103/PhysRevLett.132.206102 for details on distance calibration, data reduction, jet temperature computation, and the derivation of Eq. (2), which includes Refs. [42–47].

[42] A. G. M. Ferreira and L. Q. Lobo, The sublimation of argon, krypton, and xenon, J. Chem. Thermodyn. **40**, 1621 (2008).
[43] L. Velterop, R. Delhez, T. H. de Keijser, E. J. Mittemeijer, and D. Reefman, X-ray diffraction analysis of stacking and twin faults in f.c.c. metals: A revision and allowance for texture and non-uniform fault probabilities, J. Appl. Crystallogr. **33**, 296 (2000).
[44] E. Estevez-Rams, M. Leoni, P. Scardi, B. Aragon-Fernandez, and H. Fuess, On the powder diffraction pattern of crystals with stacking faults, Philos. Mag. **83**, 4045 (2003).
[45] https://webbook.nist.gov/chemistry/fluid/.
[46] C. Tegeler, R. Span, and W. Wagner, A new equation of state for argon covering the fluid region for temperatures from the melting line to 700 K at pressures up to 1000 MPa, J. Phys. Chem. Ref. Data **28**, 779 (1999).
[47] A. G. M. Ferreira and L. Q. Lobo, The vaporization properties of krypton and xenon, J. Chem. Thermodyn. **41**, 809 (2009).
[48] A. Niozu *et al.*, Characterizing crystalline defects in single nanoparticles from angular correlations of single-shot diffracted x-rays, IUCrJ **7**, 276 (2020).
[49] A. Niozu *et al.*, Crystallization kinetics of atomic crystals revealed by a single-shot and single-particle x-ray diffraction experiment, Proc. Natl. Acad. Sci. U.S.A. **118**, e2111747118 (2021).
[50] J. C. E, L. Wang, Y. Cai, H. A. Wu, and S. N. Luo, Crystallization in supercooled liquid Cu: Homogeneous nucleation and growth, J. Chem. Phys. **142**, 064704 (2015).
[51] C. A. Stan *et al.*, Liquid explosions induced by x-ray laser pulses, Nat. Phys. **12**, 966 (2016).
[52] M. L. Grünbein *et al.*, Observation of shock-induced protein crystal damage during megahertz serial femtosecond crystallography, Phys. Rev. Res. **3**, 013046 (2021).
[53] K. Ando, M. Arakawa, and A. Terasaki, Freezing of micrometer-sized liquid droplets of pure water evaporatively cooled in a vacuum, Phys. Chem. Chem. Phys. **20**, 28435 (2018).
[54] H. Laksmono *et al.*, Anomalous behavior of the homogeneous ice nucleation rate in "no-man's land", J. Phys. Chem. Lett. **6**, 2826 (2015).
[55] A. Kalita, M. Mrozek-McCourt, T. F. Kaldawi, P. R. Willmott, N. D. Loh, S. Marte, R. G. Sierra, H. Laksmono, J. E. Koglin, M. J. Hayes, R. H. Paul, S. A. H. Guillet, A. L. Aquila, M. Liang, S. Boutet, and C. A. Stan, Microstructure and crystal order during freezing of supercooled water drops, Nature (London) **620**, 557 (2023).
[56] C. Goy, F. Caupin, M. Caresana, L. Cremonesi, A. Kalinin, G. Grübel, M. A. C. Potenza, and R. E. Grisenti, Refractive index of supercooled water down to 230.3 K in the wavelength range between 534 and 675 nm, J. Phys. Chem. Lett. **13**, 11872 (2022).
[57] A. Tipeev (private communication).
[58] https://in.xfel.eu/metadata/doi/10.22003/XFEL.EU-DATA-002542-00